Ink Tuning for Direct Ink Writing of Planar Metallic Lattices

Lisa Biasetto,* Andy Gleadall, and Vanessa Gastaldi

316L and Cu-based inks are developed to 3D-printed tetrachiral auxetic structures. The main objectives of the work are to study the effects of powders composition and powder:binder volume ratio on rheological properties and printability of the inks. Following these results, customized Gcode is developed using FullControl Gcode Designer open-source software to 3D print intricate tetrachiral auxetic structures. The results reported in this work show how powder composition (316L versus Cu) has less effect on the inks' rheological behavior than powder size distribution and powders:binder volume ratio. In terms of rheological parameters, the zero-shear rate viscosity mainly affects the capability of the printed ink to retain its shape after printing, while the yield stress affects the printability. The printed and sintered auxetic structures achieve the intended lattice-geometry design.

1. Introduction

Additive manufacturing (AM) technologies have become a field of increasing interest to produce complex metallic structures due to the possibility of improving the design freedom and the efficiency of the produced structures.[1] Examples of applications are Ti6Al4V and 316L biomedical devices such as stents,[2] bone implants,[3–5] and thermal managing systems.[6]

Extrusion-based AM technologies are becoming more popular to produce metallic components due to the increased degree of freedom and low cost of the printing set-up, compared to powder bed fusion technologies.[7] However, they suffer some limitations related to the accuracy of the printed part and to the de-binding and sintering steps that may leave behind unwanted reaction by-products and residual porosity.[3,4,8]

In the ISO-ASTM 52 900 standard,[9] direct ink writing (DIW) is defined as an extrusion-based AM technology operated at room temperature. In DIW, a continuous flow of ink is extruded through a nozzle to deposit a spatially controlled filament of material. In the more stringent definition of DIW, the control of the shape of the printed part can be achieved by two main approaches: 1) the use of a gelling ink that naturally hardens by time or by an external stimulus such as UV light or heat at the exit of the nozzle or 2) the use of a physical gel showing a shear thinning behavior, characterized by a yield stress and a fast recovery time (in the order of tenths of seconds). Inks suitable for DIW must show a Herschel–Bulkley behavior[10] described by

$$\sigma = \sigma_Y^{Dyn} + K\dot{\gamma}^n \qquad (1)$$

where σ_Y^{Dyn} is the dynamic yield stress [Pa], K is the consistency index [Pa*s^n], $\dot{\gamma}$ is the shear rate [s^{-1}], and n is the power law exponent [-].

The control of the ink's flow and the dimensional stability after printing is a challenging issue in this technology, especially when highly loaded inks (VR > 1.2, with VR = $V_{powedrs}/V_{binder}$) are used to produce ceramic and metallic parts.

The control of ink's flow is improved when the suspension is homogenous, without air bubbles and clogging, and stable upon extrusion (i.e., no phase separation).

In highly loaded inks, the understanding of the chemical–physical properties of the ink deriving from particle–particle interaction and particle–binder interactions is a topic of great interest whose understanding will help to improve the quality of the printed parts and the upscaling of the process.[11–13]

For instance, particle size and particle size distribution, powder:binder volume ratio, particles, and binder composition, so as additives all affect the quality of the printed part, in terms of rheological behavior of the ink and consequently on flow stability and printability. Unfortunately, each ink is developed using different powders, binders, and additives so that a generalization of properties becomes challenging.

L. Biasetto
Dipartimento di Tecnica e Gestione dei Sistemi Industriali
Università di Padova
Stradella San Nicola 3, 36100 Vicenza, Italia
E-mail: lisa.biasetto@unipd.it

A. Gleadall
Wolfson School of Mechanical and Manufacturing Engineering
Loughborough University
Loughborough, Leicestershire LE11 3TU, UK

V. Gastaldi
Dipartimento di Ingegneria Elettrica
Università di Padova
via Gradenigo 6, 35131 Padova, Italy

The ORCID identification number(s) for the author(s) of this article can be found under https://doi.org/10.1002/adem.202201858.

**ADVANCED
SCIENCE NEWS**

www.advancedsciencenews.com

**ADVANCED
ENGINEERING
MATERIALS**

www.aem-journal.com

In ref. [14], the authors studied the effect of powder size and powder size distribution on the final porosity of scaffolds for Ti64 gas-atomized powder inks. Small-sized powders with a narrow size distribution (0.2–7 μm) showed struts with higher density after sintering compared to powders with a coarse powders size distribution in the range of 2–70 μm.

In ref. [12], the authors studied the effect of Y_2O_3 stabilized ZrO_2 inks with different powder size distribution and Y_2O_3 content. In this case, the variation of ink rheological properties (increase of viscosity, yield stress, and G' in the linear viscoelastic region) was attributed to the increase of Y_2O_3 content; however, there was also a decrease in powders size distribution (3 wt% Y_2O_3-d_{90} = 1090 μm; 8 wt% Y_2O_3-d_{90} = 43 μm).

Both in refs. [12,14], Pluronic F127 in distilled water was used as binder: in this case, a highly temperature-dependent hydrogel is formed.[15] More specifically, Pluronic F127, the trademark for PEO_{100}-PPO_{65}-PEO_{100} copolymer (with PEO = PolyEtylenOxide, PPO = PolyproPylenOxide) behaves like a liquid at low temperature (T = 5 °C) and like a gel at body temperature (T = 37 °C) for concentration exceeding the 20% w/w.[16]

In ref. [13], we studied the effect of binder composition on the rheological behavior of AISI 316L (gas atomized, d < 10 μm) inks: the binder was composed of two water-soluble polymers (polyethilenglicole, PEG and polyvinilalcohol, PVA) mixed at different polymer:water weight ratios and with similar PEG:PVA weight ratios. Both inks showed a shear-thinning behavior with a yield stress, with zero-shear stress viscosity, and yield stress increasing at increasing VR.

In this work, we will focus on DIW of highly loaded metallic inks with the aim of studying the effects of powders size distribution, powder composition (AISI 316L and copper), and powder to binder volume ratio on the flow stability and printability. After rheological characterization, inks will go through calibration tests to define the printing parameters suitable for the specific inks. AISI316L and copper were chosen with the main aim of comparing high density powders (7.9 and 8.1 g cm^{-3}, respectively) with a low oxidation rate.

The calibration of the printing set-up is a critical additional step for a successful printing: proper setting of printing parameters promotes constant flow and avoids swelling after extrusion, to achieve a well-controlled line width. When intricate structures are printed, the specific sequence, direction, and printing conditions for each printed line are important to consider, to achieve the intended shape of the final component. The conventional approach of slicing a CAD model and automatically determining a print path for each layer limits the potential to control these factors.[17] Therefore, recent open-source software was developed to allow direct generation of the toolpath and control all aspects of it. This means the printed lines, as well as nonprinting travel movement of the nozzle or sacrificial printed sections, can be explicitly designed and controlled to maximize quality and achieve more intricate scaffolds, where each strut is produced by a single extruded line.

This case study, focused on DIW of metallic 2D auxetic structures, requires effective linking of ink composition, ink rheological properties, and printing procedure design. A similar attempt was presented in ref. [18] with a focus on ceramic inks. Successful printing of auxetic 2D tetrachiral structures shows how the proper combination of inks' rheological properties and printing parameters allows intricate printed parts. The de-binding and sintering of the printed parts will be presented as a proof of concept of the completion of the process. Following our previous studies on printed auxetic structures by laser powder bed fusion, PBLF,[19] we here want to explore the challenges associated with 3D printing metallic auxetic structures using DIW.

In specific examples, the negative Poisson's ratio typical for auxetic structures, significantly increases mechanical properties and is beneficial for many engineering, medical, fashion and sports applications. Chiral auxetic structures represent a specific subset of auxetic structures characterized by the presence of nodes (usually circles or other geometries) and straight struts. The number of struts connected to one node defines the nomenclature of the chiral structures. Theoretical and experimental investigations show that the Poisson's ratio can reach values close to −1 in the elastic region.[20] In our previous work,[19] we studied the mechanical properties of both tetra- and hexachiral structures 3D printed by SLM using AlSi10Mg and AISI316L. Experimental and computational analysis highlighted the following points: the transverse vs axial strain relationship showed the lowest Poisson's ratio of −0.17 and −0.74 for tetra and hexachiral structures, respectively. The auxetic behavior (Poisson's ratio) can be tailored with the changing ligaments and node thickness, where the increase in the thickness results in less evident auxetic behavior. In contrast, the increase of the ligaments and nodes thickness increase the normalized maximum force. The change in the node thickness, while keeping the ligament thickness constant, results in comparable maximal force and significant increase/decrease of auxetic behavior when increasing/decreasing node thicknesses. Following these results, we want here to experiment the use of an extrusion-based 3D printing technology to 3D print chiral structures with the aim of comparing the final properties of the produced structures. This work represents the first steps toward the production of auxetic structures by DIW, this offering the advantage of avoiding postprocessing and the possibility to 3D multimaterial structures.

2. Experimental Section

2.1. Ink Preparation

AISI316L stainless steel gas atomized powders of d < 10 μm (d_{10} < 5.2 μm; d_{50} < 7.1 μm; d_{90} < 10.1 μm), d < 32 μm

Table 1. 316L Powders composition as from producer's technical datasheet.

Composition [wt%]	316Ld10	316Ld32
Chromium	16.98	16.87
Nickel	10.59	10.11
Silicon	0.47	0.34
Molybdenum	2.18	2.07
Manganese	0.84	1.83
Carbon	0.02	0.02
Iron	balance	balance

**ADVANCED
SCIENCE NEWS**

www.advancedsciencenews.com

**ADVANCED
ENGINEERING
MATERIALS**

www.aem-journal.com

($d_{10} < 9.4\,\mu m$; $\quad d_{50} < 16.1\,\mu m$; $\quad d_{90} < 24.6\,\mu m$), and $\rho = 7.79\,g\,cm^{-3}$ were purchased from Eckart TLS GmbH and used as received.

The chemical composition of powders as from producer datasheet is reported in **Table 1**.

Cu gas atomized powders of $d < 35\,\mu m$ ($d_{10} < 10.3\,\mu m$; $d_{50} < 19.8\,\mu m$; $d_{90} < 30.1\,\mu m$), $\rho = 8.96\,g\,cm^{-3}$, composition Cu 99.95% were purchased from Eckart TLS GmbH and used as received. Powders densities were measured by He-Pycnometry (UltraPyc 3000, Anton Paar).

The inks were prepared by mixing metallic powders and a water-based solution of polymers, as previously reported in ref. [13]. Different powder over binder volume ratios were tested as reported in **Table 2**.

The polymeric binder was prepared using Polyvinilalchol (PVA) (SigmaAldrich $M_w = 9000\text{-}10.000\,g\,mol^{-1}$, 80% hydrolized), polyethilenglycole (PEG) (Sigma Aldrich $M_n = 950\text{-}1000\,g\,mol^{-1}$), and distilled water with the following weight ratio PVA: PEG: H2O = 18.75:16.25: 65. PVA and PEG were dissolved into water at 80 °C for 2 h under magnetic stirring and then left gently cooling overnight.

A Thinky centrifugal mixer was used to mix the metallic powders with the binder using the following cycle: 2 min at 400 rpm, 2 min at 1000 rpm, and 2 min at 1200 rpm followed by defoaming at 400 rpm for 2 min. The ink was kept inside a cooled container to prevent overheating upon mixing. Binder's density was estimated by the rule of mixture.

2.2. Inks' Rheological Characterization

Rheological properties were measured at room temperature ($T = 25$ °C) with the aim of quantifying the physical properties affecting the printability of the produced inks.

A plate-plate rheometer ($d = 20\,mm$) (Netzsch, Kinexus) with solvent trap under water was used. Large amplitude oscillatory shear stress (LAOStress) measurements[21] were performed at controlled shear stress in the range 1-1000 Pa or 1-3500 Pa at 0.5 Hz with a 0.4 mm gap. The log–log plot of complex viscosity versus shear stress was used to define the rheological behavior of the inks. By mean of storage modulus G' and loss modulus G'' versus shear stress log–log plots the following parameters were determined[22]: the storage modulus in the linear viscoelastic region LVR, G'_{LVR} [Pa], the stress at the crossover point τ_f where G'=G'', and the flow transition index FTI (dimensionless), defined as the ratio between the stress at the crossover point τ_f, and the stress at the yield point τ_y (G'=0.95 G'_{LVR}).

The crossover point defines the step over which the viscous behavior overcomes the elastic behavior, meaning that the ink's structure is partially destroyed by the acting shear stress.

The thixotropic properties of the inks with VR01.3 were measured by means of a three steps recovery test at controlled shear stress: a stress, of 0.1 and 100 Pa, was applied for 30 s, and finally the viscosity recovery was monitored with a stress of 0.1 Pa for 600 s.

2.3. Calibration of the Printing Set-Up

To correlate the rheological parameters extracted by LAOSstress measurements with the effective printability of the inks, a printing test was designed with the open-source software Fullcontrol-GCode Designer.[23] The printing paths were directly designed and used to generate GCode suitable for the 3D printing machine.

A commercially available Delta 3D printer WASP 2040 Clay (WASP, Massa Lombarda-Ravenna, Italy) was modified by connecting an endless piston ViproHead3 extruder produced by ViscoTec Pumpen Dosiertechnik GmbH (Toging, Germany) to which extremity a LuerLock 410 μm conical nozzle was connected (Nordson). Printing experiments were run at conditioned environmental temperature of 22°±1 °C.

Extrusion occurred at room temperature, and it was affected by the following printing parameters: the extrusion length E [mm per printed line], the nozzle displacement speed F [mm/min], the printed part length L [mm], the printing distance Z [mm] (defined as the distance between the nozzle tip and the printing plate), the interlayer distance h [mm], and the nozzle diameter d [mm].

During calibration, the printing distance Z, the interlayer distance h, and the nozzle diameter d were kept constant ($Z = 349.7\,mm$, $d = 410\,\mu m$, and $h = 0.6\,d$), while the other parameters were varied according to **Table 3**, where the deposition speed v [mm sec^{-1}] was defined as follow (Equation (2))

$$v = \frac{E*F}{L} \tag{2}$$

The width of the printed lines (see **Figure 1**) was measured by a stereo-microscope (STEMI 2000-C, Carl Zeiss AG, Oberkochen, DE), at least three measurements for each block were taken, from which the average and standard deviation were calculated. From the collected data, it was possible to define the effect of deposition speed v on the line width, so as the effect of the printing parameters by mean of the partial derivative of the deposition speed $\frac{\partial v}{\partial E}$, $\frac{\partial v}{\partial F}$.

By mean of this procedure, it was possible to define the most appropriate combination of ink and printing parameters to produce the tetrachiral structure, which would not be possible otherwise.
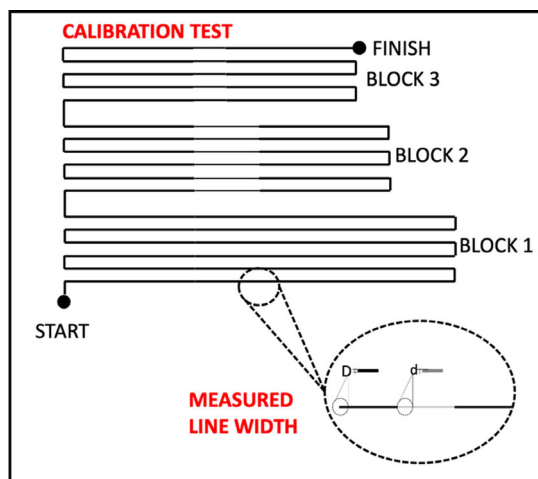
Table 2. Inks' composition overview (VR = Volume Ratio).

Sample Labelling	Metallic Powder [wt%]	Binder [wt%]	Metallic Powder [vol%]	Binder [vol%]	VR[a]
316L10 VR1.2	90.0	10.0	54.81	45.19	1.21
316L10 VR1.4	91.0	9.0	57.68	42.32	1.36
316L10 VR1.5	92.0	8.0	60.78	39.22	1.55
316L32 VR1.2	90.0	10.0	54.35	45.65	1.19
316L32 VR1.3	91.0	9.0	57.22	42.78	1.34
316L32 VR1.5	92.0	8.0	60.34	39.66	1.52
Cu35 VR1.3	92.0	8.0	57.40	42.60	1.35
Cu35 VR1.6	93.0	7.0	60.89	39.11	1.56
Cu35 VR1.8	94,0	6,0	64.74	35.26	1.84

[a]VR = Volume Metallic Powders/Volume Binder.

Figure 1. Example of calibration test design and measured lines widths, *D* and *d*.

2.4. 3D Printing of Tetrachiral Structures

The tetrachiral structure was designed with the parameters reported in **Figure 2**.

The designed properties were designed using Fullcontrol GCode open-source software[23] following the workflow reported later.

Given the challenges of starting and stopping extrusion for highly loading inks, the print path was designed to allow continuous extrusion without the need for nonextruding fast-travel movement of the nozzle, which would normally be unavoidably included if this structure was printed using the conventional AM workflow with a CAD model and slicing software. The print path was parametrically adjustable in terms of unit cell size and number of unit cells along the length and width of the specimen. It is shown in **Figure 3**. To avoid the nozzle traveling over previously printed lines, sacrificial lines were printed around the structure when it was necessary to move the nozzle from one position on the outer edge of the specimen to another position on the outer edge. Since the specific lattice structure studied here cannot be printed continuously in one pass without nonextruding fast-travel movements, or printing over the same line twice, the toolpath was designed with a four-stage approach. Each stage printed half of the straight-line
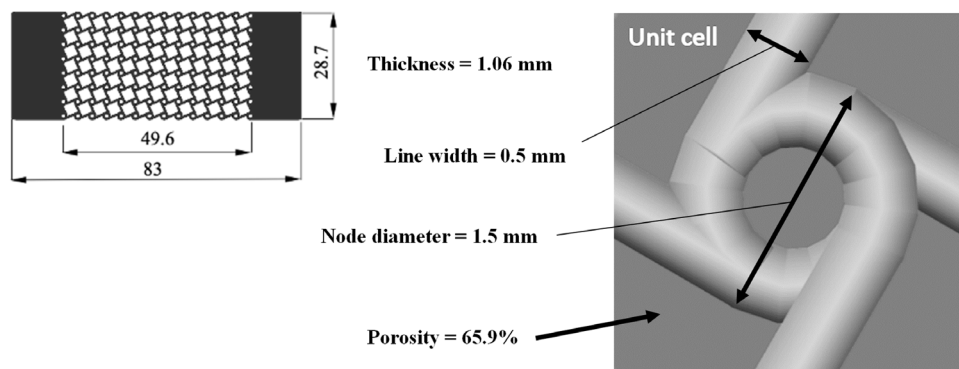
connections between circles for a single layer and is therefore considered to be a half-layer, even though it is printed at the full layer height. The print path for a single unit cell for the first half-layer ("Layer 1-1") is shown in the bottom left of the figure, with a preview of the overall half-layer shown immediately below it. The next half-layer ("Layer 1-2") is shown next to it. As can be seen, all straight-line struts have been printed after the first two half-layers, along with the grip regions at the left and right of the specimen. However, some of the circle section of the unit cell has not been printed after the first two half-layers. The next two half-layers ("Layer 2-1" and "Layer 2-2") complete the circle sections as well a print the straight lines sections a second time. Therefore, after four half-layers, two layers have been printed for every part of the structure. This path design allows the lattice struts to be printed with the width of a single printed line, which is the best possible resolution for this process. Conventional slicers typically print a minimum of two lines for each feature in a geometric structure, as discussed later in this paper, and therefore do not achieve the best possible resolution, that can be achieve by explicitly designing the print path with FullControl GCode Designer.

2.5. De-Binding and Sintering

To convert the printed structure into a dense metal structure, it is necessary to remove the binder and to sinter the metallic powders. The most appropriate way to reach this goal with the binder developed in this work is thermal de-binding and sintering.

We referred to previously reported data of TGA-DTA analysis and previous results of sintering[13] to define the thermal treatment for 316 L samples. In particular, we used the following cycle under argon atmosphere: $0.5\,°C\,min^{-1}$ to $500\,°C$, dwelling 1 h, and $2\,°C\,min^{-1}$ up to $1240\,°C$.

Cu specimens were sintered using a Markforged sintering unit (Sinter-2) with thermal cycle for copper under Ar/H_2 atmosphere (de-binding and sintering conditions are protected by Markforged).

2.6. Specimens' Characterization

Scanning electron microscopy analyses were performed using a SEM-FEG (Quant-FEI Eindhoven, Netherland) at 20 kV and 10 mm working distance. Electron dispersive spectroscopy analyses were performed using an EDS probe (ThermoScientific, Ultradry).
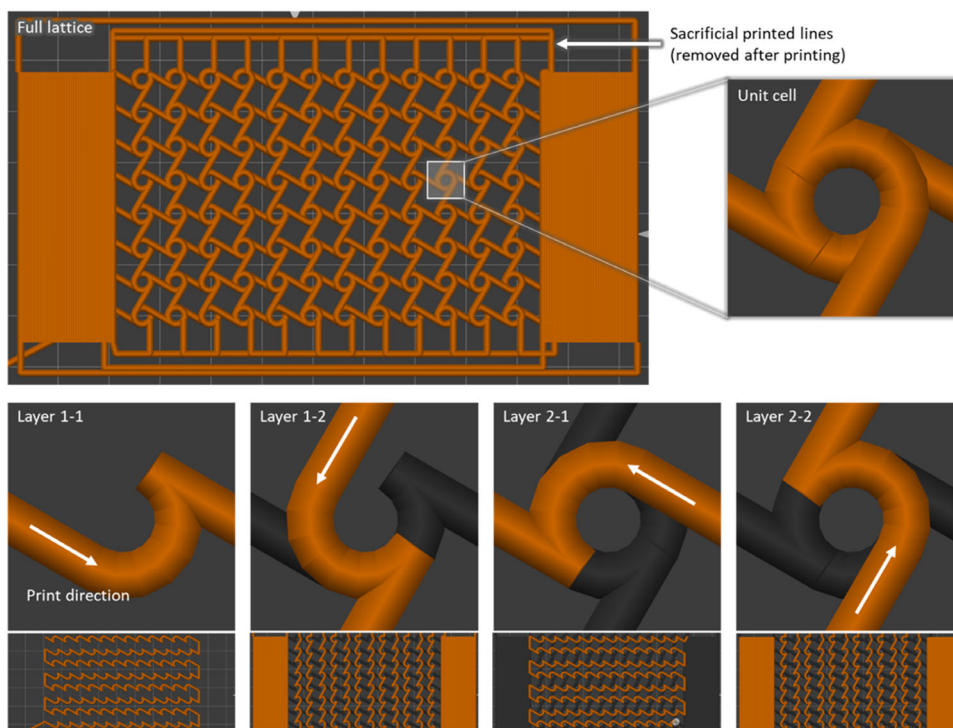

Figure 2. Specimens designed properties.

Figure 3. Print-path design for the tetrachiral lattice structure. Neat printing at the best possible resolution was enabled by designing the print-path in FullControl GCode Designer as a sequence of four half-layers. Sacrificial material was printed outside the region of interest to avoid defects that often occur when a nozzle travels over previously printed sections.

3. Results and Discussion

In **Figure 4**, SEM analysis of as received powders is reported.

As can be observed, 316L10 and 316L32 powders show a spherical regular shape and a smooth surface, while the Cu powders show a rougher surface.

3.1. Rheological Properties

The inks' rheological characterization by mean of stress-controlled amplitude sweep tests is reported in **Figure 5**.

The all inks show a zero-shear rate viscosity (η_0) and a decrease of viscosity after a shear stress threshold (Figure 5a–c top). Both inks prepared using 316L10 and 316L32 powders show a lower value of η_0 for VR of 1.2, compared to inks with VR > 1.2. Cu-based inks with VR of 1.3, 1.5, and 1.8 show a similar trend of η_0 values. The analysis of G' and G'' versus shear rate graphs (Figure 5a–c, bottom) allows to identify the values of yield stress (σ_y) and flow stress (σ_F), so as the FTI value defined as ratio between σ_F and σ_y.

In **Figure 6**, an overview of the σ_y and FTI values is reported as function of VR for all inks prepared in this work.

The effect of powder size on the ink strength is clearly visible comparing the values of σ_y for 316L10- and 316L32-based inks, Figure 6a. At increasing VR, the σ_y values increase following a parabolic trend for 316L10-based inks. In inks prepared using larger powders size, σ_y is not affected by VR for VR < 1.6 as
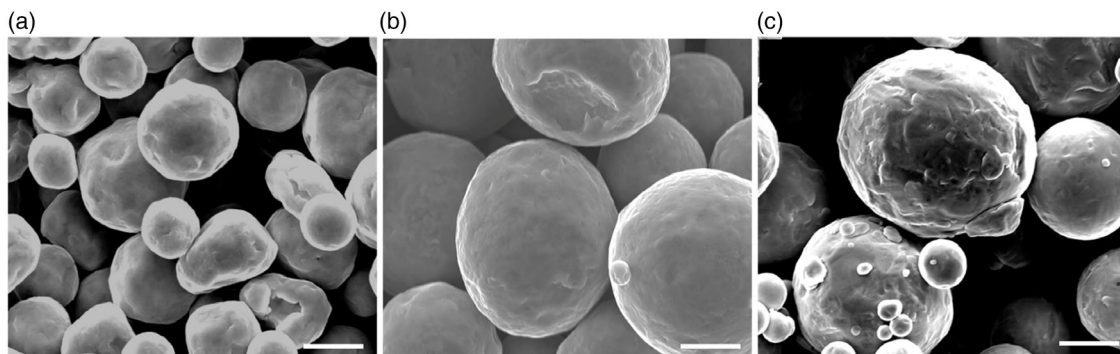

Figure 4. SEM (secondary electrons) images of as received powders: a) 316L10, b) 316L32, and c) Cu35, scale bar 5 μm.

**ADVANCED
SCIENCE NEWS**

www.advancedsciencenews.com

**ADVANCED
ENGINEERING
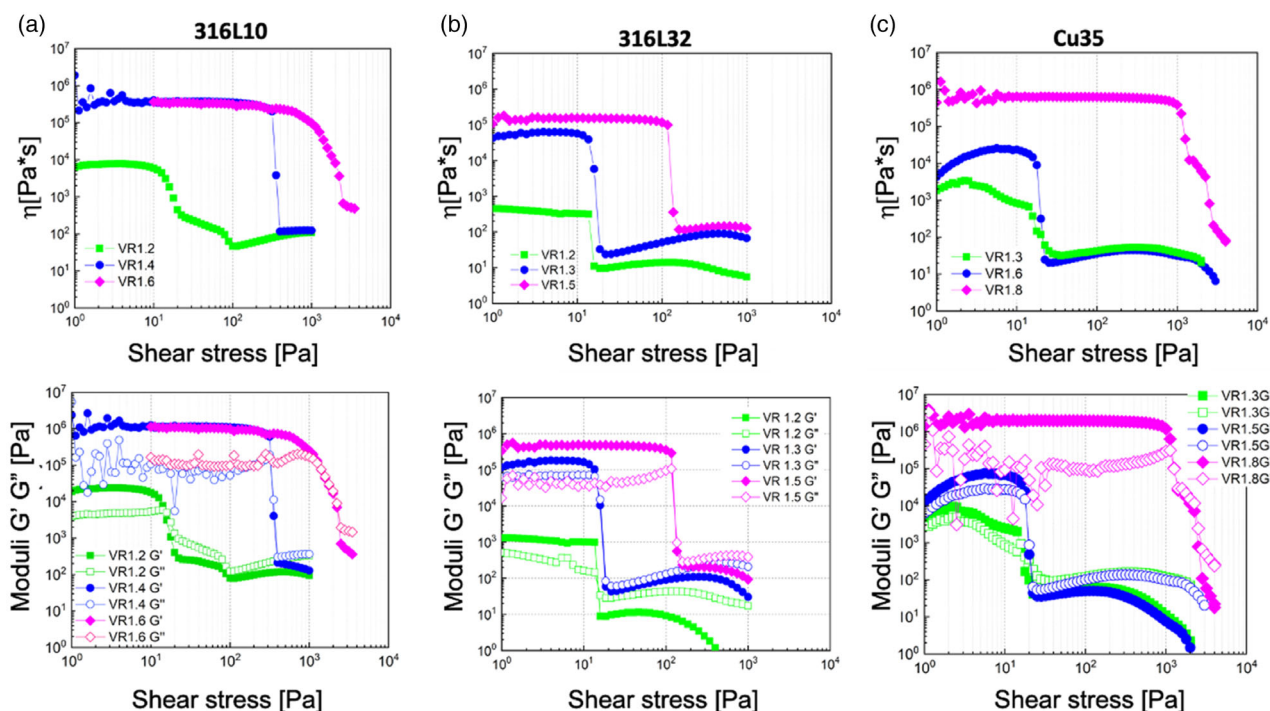MATERIALS**

www.aem-journal.com

Figure 5. Viscosity versus shear stress and moduli G' and G'' versus shear stress for all inks: a) 316L10-based inks; b) 316L32-based inks; c) Cu35-based inks.
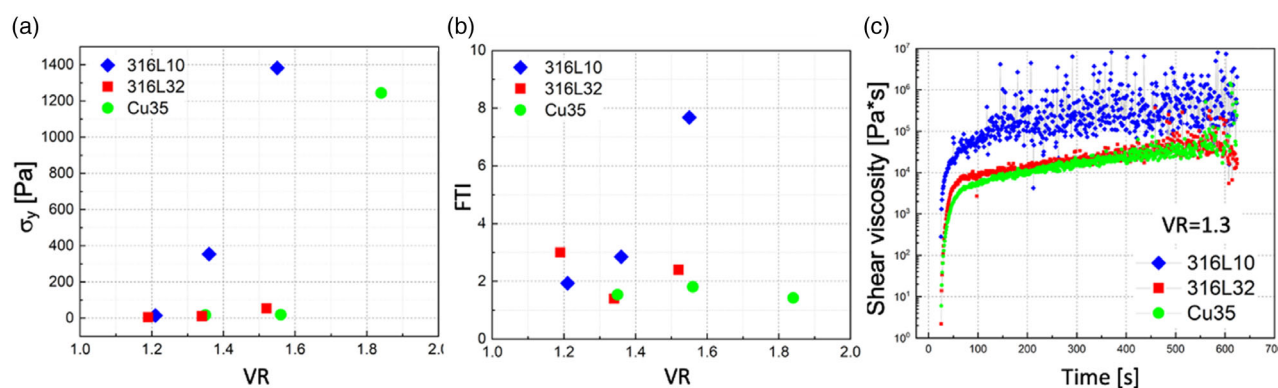

Figure 6. Effect of inks composition in terms of VR on a) σ_y, b) FTI and c) thixotropy test.

confirmed by Cu35-based inks. Composition (316L32 vs Cu35 powders) seems to affect less significantly the yield of the ink than powder size (316L10 vs 316L32). FTI values, reported in Figure 6b, show a similar trend to σ_y values for 316L10 inks, while for 316L32 and Cu35, a clear trend is not detectable. σ_y represents the values of stress where the elastic behavior of the inks starts to collapse, and σ_F is the point where the viscous behavior overcome the elastic one. For small powders size, a proportionality is kept between σ_y and σ_F, while for powders of larger size, the low values of FTI at all VR show that the transition between the elastic and viscous behavior occurs in a narrow range.

At increasing powders size, we expect fewer binder–powder interactions thus weakening the inks' structure. In inks prepared

using Cu35, for VR > 1.6, the powder–binder interactions become comparable to those prepared using smaller powders size of different composition (Figure 6a). The measurement of powders wettability could represent a significant improvement for the understanding of powder–binder interaction[18]: in the work by M'Barki and co-worker, authors proposed a unified parameter to decline the printability of ceramic-based inks depending on the ratio between yield stress and the sum between binder–particle surface energy and gravitational force. For high values of surface energy, the printability becomes depending only by the ratio between yield stress and surface energy.

The study of thyssotropic properties of the inks also represents an important parameter in defining the quality of the printed part. An overview of recovery time for inks prepared with

316L10, 316L32, and Cu35 at VR = 1.3 is reported in Figure 6c. Recovery times are similar for the three inks, while the final viscosity is confirmed to be at least one order of magnitude higher for 316L10 ink. This can be attributed to the increasing number of particle–binder–particle interactions. Binder covers the surface of the particles and bridges particles one to each other. The number of bridges is increased at decreasing particle size.

3.2. Printing Calibration

Printability tests showed that the produced inks exhibited three distinct behaviors: printable but nonmeasurable, printable and measurable, and nonprintable.

Inks were defined printable when a constant flow was detected; inks were defined nonmeasurable when the printed lines collapsed after the deposition to the substrate; inks were defined as nonprintable when a discontinuous flow was detected.

In Table 3, an overview of printability test and measured values of lines width is reported. It should be noted that using the printing parameters reported in Table 3, lines width always largely exceeds the nozzle size.

In **Figure 7**, an overview of the printability test is reported for inks prepared with the three metallic powders and with comparable values of VR.

The effect of powders size is clearly visible in 316 L inks with VR ≈ 1.35, while not clear differences can be detected between

Table 3. Overview of printability tests, D and d as defined in paragraph 2.3, Figure 1.

Printing Test	Block 1		Block 2		Block 3	
Extruded Length E [mm]	10	10	5	5	2.5	2.5
Deposition Speed v [mm s^{-1}]	2.5	5	1.25	5	0.625	5
Head Speed F [mm s^{-1}]	5	10	5	10	5	10
Line length L [mm]	20	20	20	10	20	5
Ink	D [μm]	d [μm]	D [μm]	d [μm]	D [μm]	d [μm]
316L10 VR1.2	1021.8 ± 47.3	753.1 ± 48.5	939.4 ± 18.2	703.8 ± 31.6	878 ± 35.5	659.5 ± 29.1
316L10 VR1.3	857.8 ± 55.6	614 ± 55.4	867.5 ± 46.4	570.8 ± 27.3	739.4 ± 50.5	557 ± 39.1
316L10 VR1.5			Not printable			
316L32 VR1.2			Printable, not measurable			
316L32 VR1.3	1407.4 ± 112.2	950.9 ± 14.7	1362 ± 126.9	982.7 ± 65.6	1350.7 ± 116.3	945.6 ± 95.1
316L32 VR1.5	951.5 ± 55	688.6 ± 44.4	872.2 ± 50.8	549 ± 10.6	745.8 ± 48.7	520.4 ± 27.5
Cu5 VR1.3	965.8 ± 48.8	755.2 ± 29.2	990.3 ± 76.1	1032.9 ± 82.3	974,9 ± 48.4	1448.1 ± 68.1
Cu35 VR1.6	724.1 ± 74.6	484 ± 57.1	839 ± 55.6	939.3 ± 93.3	856.4 ± 52.2	1310.6 ± 108.8
Cu35 VR1.8			Not Printable			

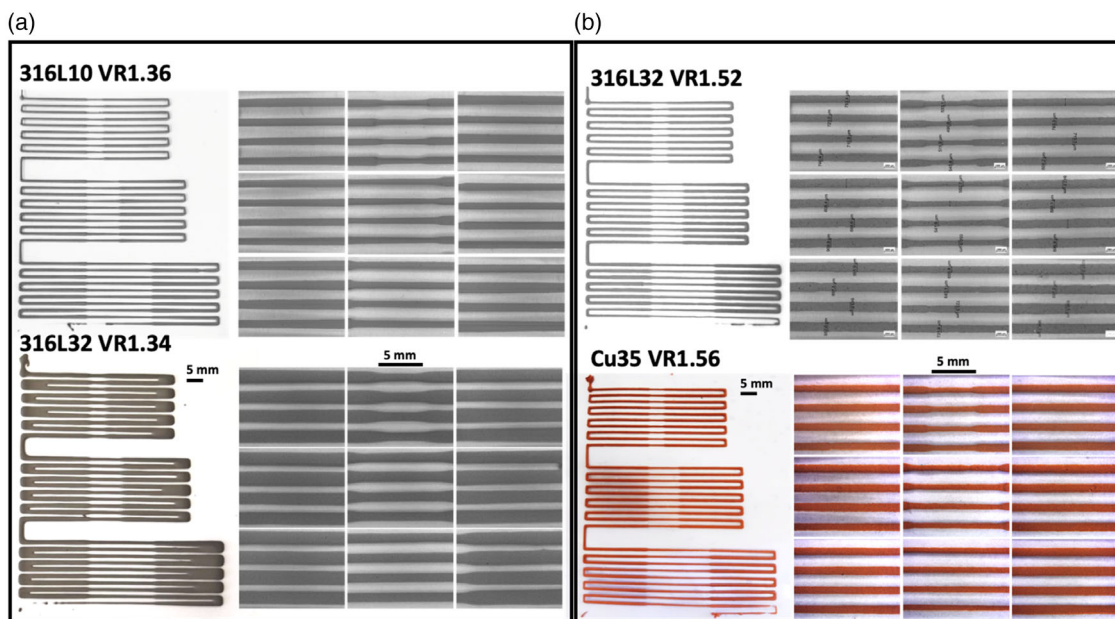**Figure 7.** Printability test: a) comparison between 316L10 and 316L32 inks, with VR ≈ 1.35; b) comparison between 316L32 and Cu35 inks with VR ≈ 1.5.

**ADVANCED
SCIENCE NEWS**

www.advancedsciencenews.com

**ADVANCED
ENGINEERING
MATERIALS**

www.aem-journal.com

316L32 and Cu35 with VR ≈ 1.5, this showing how in the case study proposed in this work, powders composition is less affecting the inks rheological properties than powders size. This is also in agreement with data reported in Figure 5. On the other hand, the effect of VR at constant powder size and composition (316L32VR1.34 vs 316L32VR1.52) is also affecting the ink quality.

The deposition speed versus line width data for all printable and measurable inks are reported in **Figure 8**.

For all inks, the parameters used for the printing calibration exceed the target line width, as also highlighted in Table 3. The linear fitting of the measured values D versus the deposition speed v in the three blocks of the calibration tests drive to the range of deposition speeds useful to get lines width comparable to the one of the used nozzle. It should also be noted that the range of target v decreases at increasing VR for the three metallic powders. This result is significant since a decrease in the range of deposition speed v for target line width D can be associated to a more homogeneous ink and consequently to a more constant flow.

To determine the most dominant parameter affecting the line width partial derivative of deposition speed v were analyzed as reported in **Figure 9**.

From the study of partial derivatives, the following observations can be highlighted: for 316L10 VR1.2, a linear trend can be detected for $\delta v/\delta F$ showing that the line width can be better controlled by mean of printing head speed F. This linear trend is not confirmed for 316L10 VR1.4, 316L32, and Cu35 inks, which, however, show a variation of lines widths associated to the variation of F. As concern the effect of extrusion parameter E, it seems clear that for values of $\delta v/\delta E > 0.5 \; sec^{-1}$ the line width is not affected by the extrusion length E, this meaning that at constant F over L ratio low values of E do not affect the line width. These

considerations become important when the printing path is tortuous and line widths need to be strictly controlled to grant for an optimized printing accuracy, as is the case of auxetic structures.

Printing accuracy is the result of the proper setting of printing parameters (v) and ink rheological properties (σ_y, σ_f, and η_0). In **Table 4**, an overview of rheological properties and printability test is reported. For 316L10 inks, a clear trend is detected where high values of FTI (7.7) and $\sigma_y = 180$ Pa drive to not-printable ink. 316L32 inks show that low values of η_0 drive to not measurable inks (lines overlapping). Cu35-based inks show a different trend where low values of FTI (1.4) and high values of σ_y (872 Pa) drives to not printable inks. From the above considerations, for highly loaded inks made of metallic powders, the parameter most affecting the printability is σ_y. The stability of the printed path can be associated to the values of η_0. These experimental observations show how the rheological behavior of metallic inks is different from the one observed in ref. [23] using polymeric inks or in ref. [16] where ceramic inks were studied. Differences may be attributed to the binder–powder interactions.

3.3. Printing Tetrachiral Auxetic Structures

Following the above considerations, 316L10 inks and Cu35 inks were selected to print auxetic structures. In **Figure 10** and **11**, images correlating the printability test and the printed auxetic structures are reported.

For 316L10 VR1.2 and for Cu35VR1.3 inks an overflow is detected, causing an excessive thickening of the struts and nodes. The two compositions 316L10 VR1.3 and Cu35 VR1.6 show a good adhesion to the design constraints and for this reason they were selected to print the auxetic structures.

De-binded and sintered structures are reported in **Figure 12**a,b as example of how the process can be completed. Some cracks are
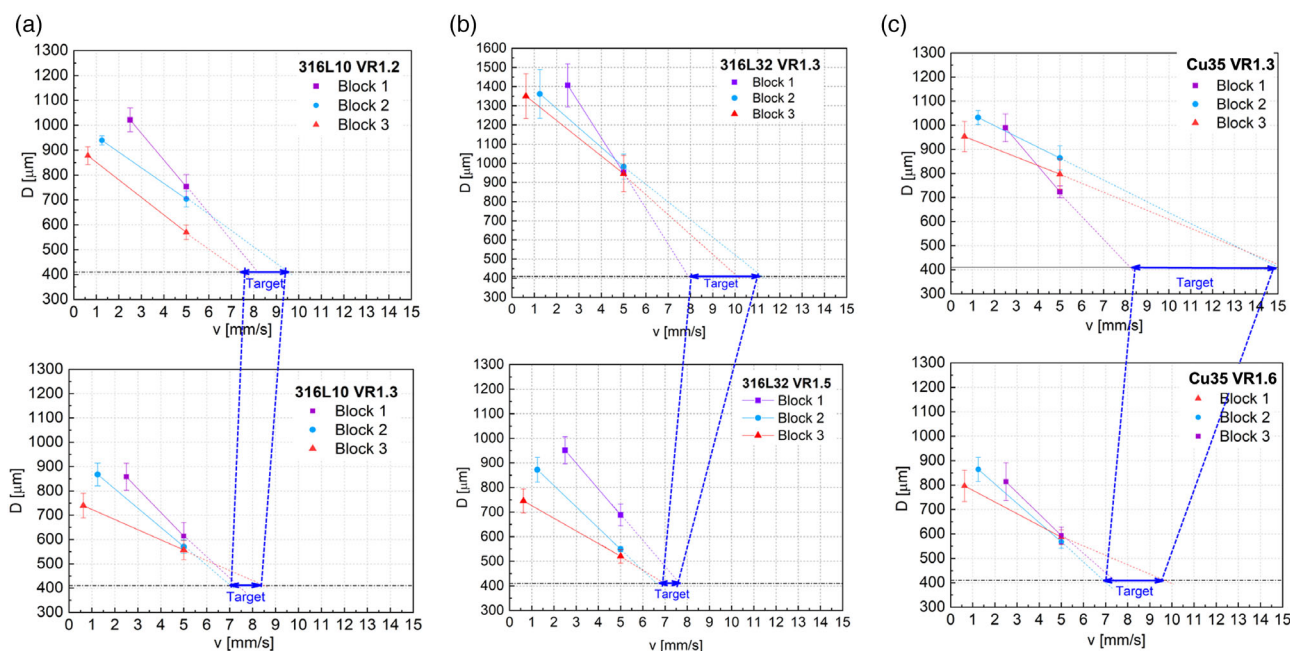

Figure 8. Measured lines width D versus deposition speed v for all printable and measurable inks: a) 316L10, b) 316L32 and c) Cu35. The target line width is highlighted in a range of deposition speeds.
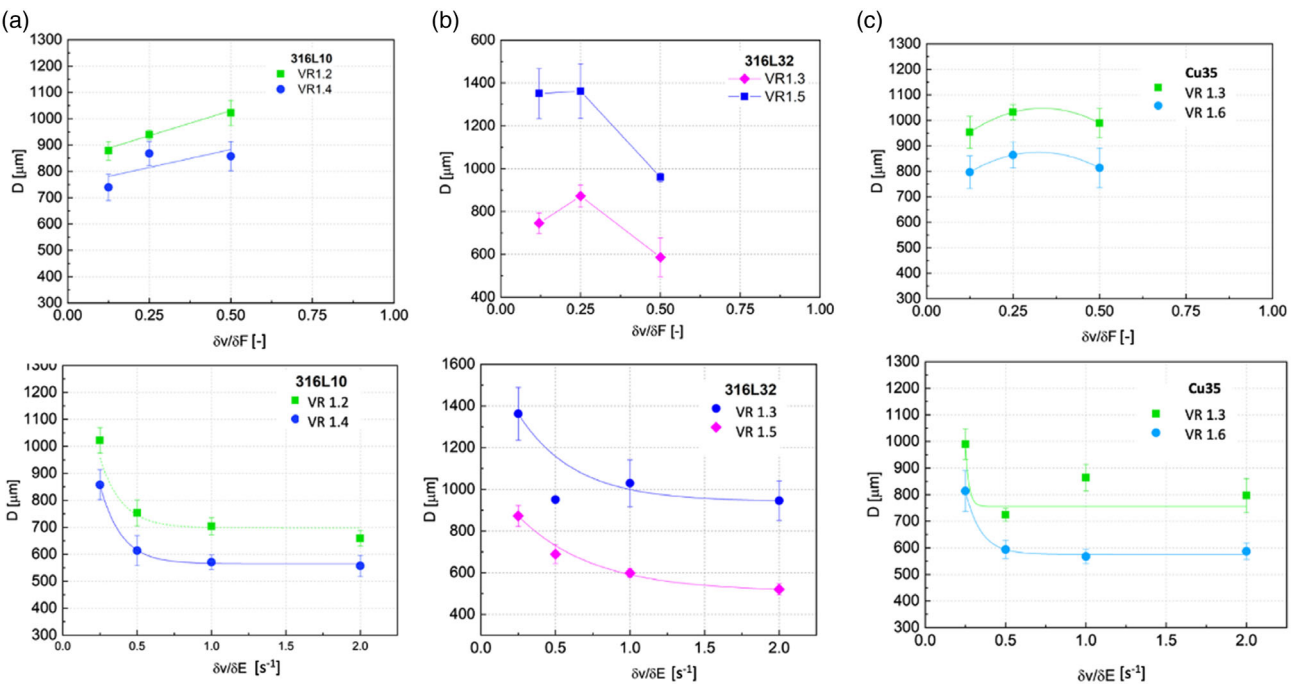
Figure 9. Lines' width D versus v partial derivative for printable and measurable inks: a) 316L10, b) 316L32 and c) Cu35. Interpolation lines, when present, only reported to drive the eye.

Table 4. Rheological parameters and printability.

	η_0 [Pa*s]	σ_y [Pa]	σ_F [Pa]	FTI	Printability
316L10 VR1.2	8700	7.8	15.1	1.9	Printable
316L10 VR1.4	330 000	124	354.2	2.8	Printable
316L10 VR1.6	340 000	180	1382	7.7	Not printable
316L32 VR1.2	376	14.9	4.9	3	Printable, not measurable
316L32 VR1.3	62 928	14.8	10.6	1.4	Printable
316L32 VR1.5	151 074	129	54.2	2.4	Printable
Cu35 VR1.3	1846	11.4	17.5	1.5	Printable
Cu35 VR1.6	24 933	10.6	19.2	1.8	Printable
Cu35 VR1.8	64 898	872	1243.5	1.4	Not printable

visible both on 316L10 VR1.3 and Cu35 VR1.6 at the node-strut junction. We expect that such cracks were caused by samples handling before sintering more than the sintering process itself. In Figure 12c, the measured values of ligament thickness (struts) and inside and outside diameter are reported. A good match with the design constraints can be observed after sintering, with similar values of shrinkage except for node inside diameter of Cu35 structure. This point is still not clear.

SEM images of the sintered 316L10 VR1.3 and Cu VR1.6 samples are reported in **Figure 13**. The printing path used to fill the volumes is clearly visible for 316L10 VR1.3, Figure 13a, while it is less evident for Cu VR1.6, Figure 13d; this can be due to the lower values of zero shear stress viscosity (see Table 4).

Surface is following the intrinsic roughness due to the used 316 L and Cu gas atomized powders. Steel samples are forming the sintering neck, but still preserve their original shape, Figure 13b,c. Cu samples on the other hand show that sintering treatment is not effective, Figure 13e,f.

We here also report as comparison the morphology of 3D-printed auxetic stainless steel structures by LPBF[19] and both steel and Cu structures using a Markforged FFF printer, de-binding, and sintering unit (**Figure 14**). In the case of FFF, the filament feedstock material, printing process, and thermal treatment are all controlled by the Markforged software, and only few details are available: nozzle temperature 210 °C, room and plate temperature 65 °C, chemical debinding in ultrasounds using Opteon SF-79; thermal debinding and sintering were performed using the Sinter2 unit under Ar/H$_2$ atmosphere with the thermal cycle optimized for steel and copper, respectively.

However, we think that the comparison is useful to understand the limits of the different available technologies. The use of LPBF gives a very well-defined structure with intrinsic roughness due to the laser melting process (Figure 14a), on the other hand, FFF gives a more squared structure with the node dimensions decreasing compared to the design. In addition, holes are visible partly on the bottom and more clearly on the top of the node for the steel structure (Figure 14b,c). This is because the software utilized a conventional print-path generation procedure whereby a CAD model is inspected, and lines are printed where the surface of the solid volume exists in the model. This means that each strut is printed by two lines side-by-side instead of being printed by a single line, as is possible when the toolpath is explicitly designed as it was for the other specimens in this study.
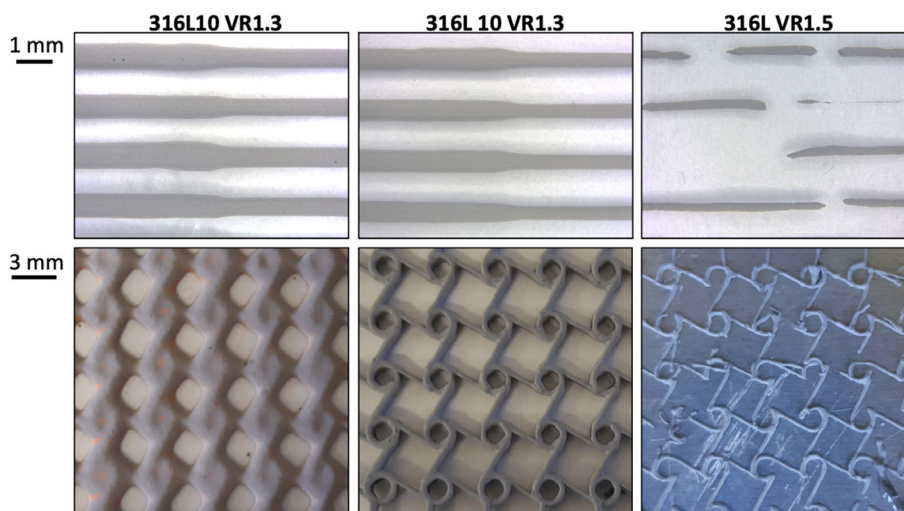
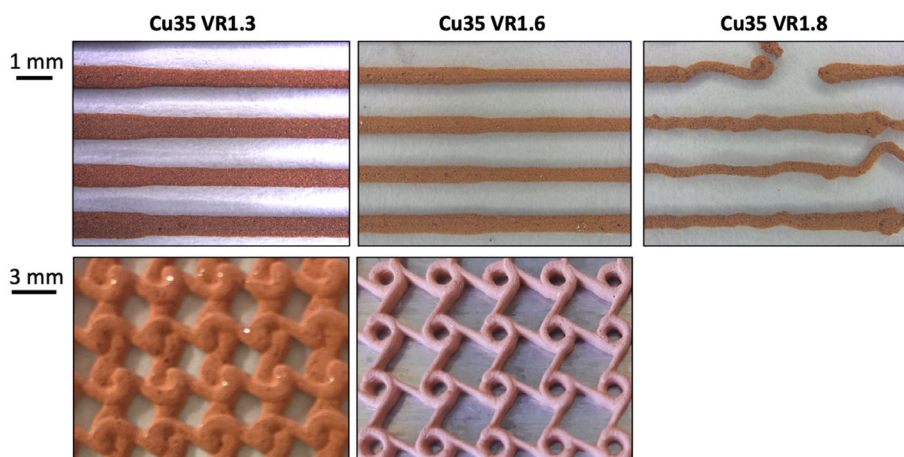**Figure 10.** Printing tests and one layer printed auxetic structures for 316L10 inks.

Figure 11. Printing tests and one-layer printed auxetic structures for Cu35 inks.

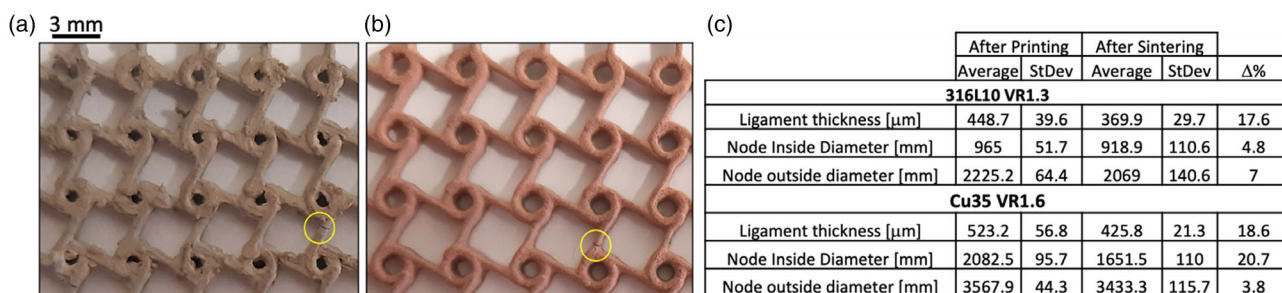|	After Printing		After Sintering		
	Average	StDev	Average	StDev	Δ%
316L10 VR1.3					
Ligament thickness [μm]	448.7	39.6	369.9	29.7	17.6
Node Inside Diameter [mm]	965	51.7	918.9	110.6	4.8
Node outside diameter [mm]	2225.2	64.4	2069	140.6	7
Cu35 VR1.6					
Ligament thickness [μm]	523.2	56.8	425.8	21.3	18.6
Node Inside Diameter [mm]	2082.5	95.7	1651.5	110	20.7
Node outside diameter [mm]	3567.9	44.3	3433.3	115.7	3.8

Figure 12. De-binded and sintered 316L10 VR1.3 a) and Cu35 VR1.6 b); c) measured geometrical values after printing and after sintering.

For Cu samples holes on the node are missing, and the effect can be attributed to the fact that nozzle temperature is more effective in softening the Cu filament.

Parametric design with a full control of the G-code generation combined with DIW of metallic inks represent a first attempt to use DIW to 3D print 2D auxetic structures. Following topology optimization studies and computational modeling results,[24–26] different negative Poisson ratio materials can be produced. Auxetic polymer lattices were recently 3D printed by one of the authors[27] to achieve a wide range of positive and negative
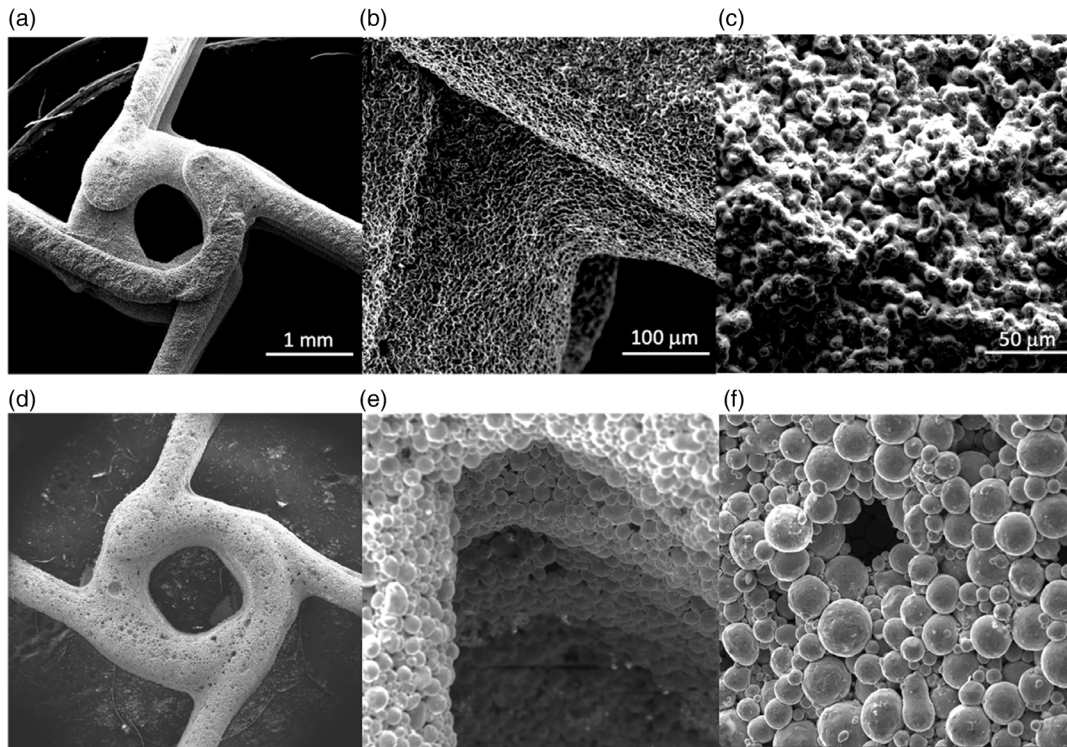
Figure 13. Backscattered SEM image of a tetrachiral node of 316L10 VR1.3 sample after sintering: a) second layer, node, and struts; b) detail of two consecutive layers; c) detail of the surface. d) Cu 35 VR1.6 second layer, node, and struts; e) detail of two consecutive layers; f) detail of the surface.
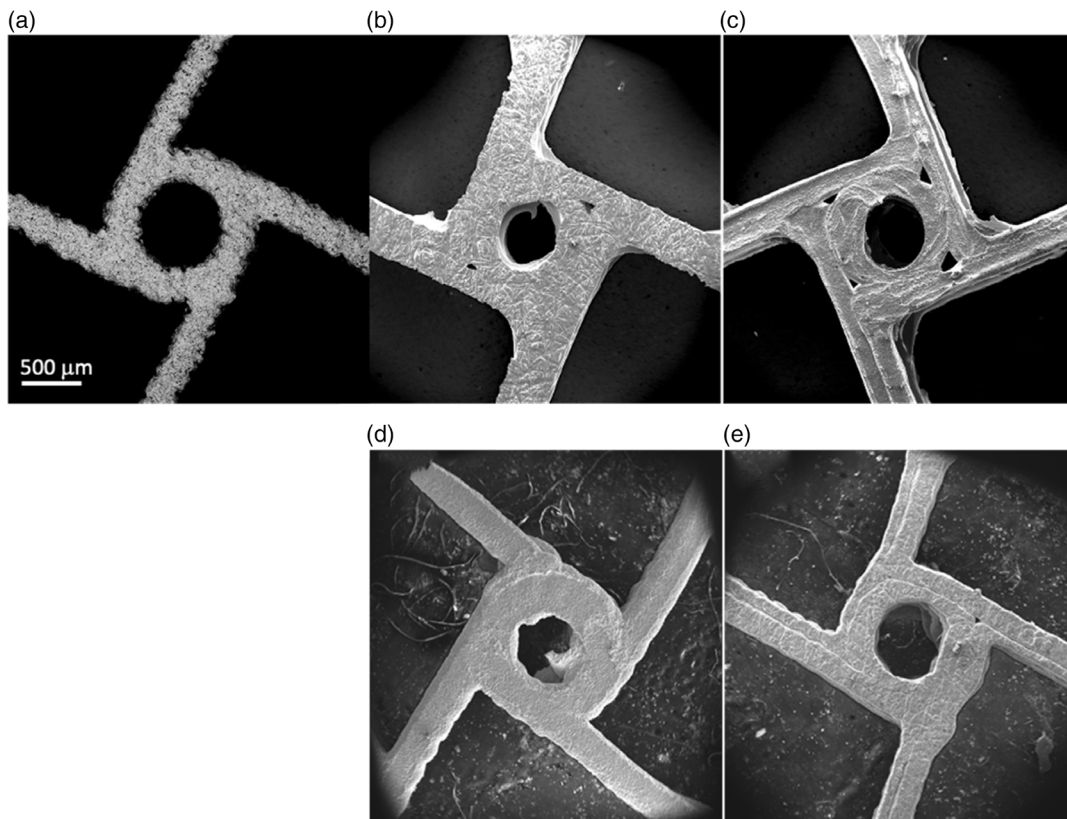

Figure 14. a) PBLF-printed 316L[17]; b) FFF-printed 17-4 PH stainless steel top, c) bottom, d) FFF printed Cu top, e) bottom, scale bar 500 µm for all images.

values for Poisson's ratio using the same software for toolpath design as was used in this study. Those structures are appropriate for DIW of metallic inks and would be in interesting direction for future research.

4. Conclusions

316 L and Cu inks were developed to 3D print by DIW tetrachiral auxetic structures.

Inks' rheological properties were related to printing parameters, which were explicitly controlled along with all other aspects of the print-path using Fullcontrol Gcode Designer software.[23]

Main results can be summarized in the following points: 1) Inks realized with 316 L powders size $d < 10\,\mu m$ show the printability limit in terms of volume ratio in the range $1.2 < VR < 1.6$. At increasing powder size, the printability limit is moved to higher values $1.3 < VR < 1.8$. The effect of VR can be associated to an increase of zero shear rate viscosity η_0 and to yield stress σ_y. 2) The effect of powders composition limited to the specific comparison between 316L and Cu on inks rheology and printability is less evident. At this point of the study, it is not possible to generalize conclusions on different metallic alloys: density and oxidation of the gas atomized powders could affect powder-binder wettability and consequently ink rheological properties. These parameters need to be specifically investigated. 3) Auxetic structures were successfully printed using 316L10 VR1.3 and Cu35 VR1.5. Lines width and nodes after printing and sintering showed a good matching with design constraints. 4) Compared to tetrachiral structures printed with PBLF and FFF, the 4-chiral structures printed by DIW show a more intricate deposition path, whose effect is under study in terms of mechanical response.

Conflict of Interest

The authors declare no conflict of interest.

Data Availability Statement

The data that support the findings of this study are available from the corresponding author upon reasonable request.

[1] D. Svetlizky, M. Das, B. Zheng, A. L. Vyatskikh, S. Bose, A. Bandyopadhyay, J. M. Schoenung, E. J. Lavernia, N. Eliaz, *Mater. Today* **2021**, *49*, 271.

[2] C. Wang, L. Zhang, Y. Fang, W. Sun, *Engineering* **2021**, *7*, 979.

[3] H. Elsayed, N. Novak, M. Vesenjak, F. Zanini, S. Carmignato, L. Biasetto, *Mater. Sci. Eng., A* **2020**, *787*, 139484.

[4] M. Coffigniez, L. Gremillard, S. Balvay, J. Lachambre, J. Adrien, X. Boulnat, *Addit. Manuf.* **2021**, *39*, 101859.

[5] H. Qian, T. Lei, P. Lei, Y. Hu, *Tissue Eng. Part B* **2021**, *4*, 166.

[6] T. Dixit, E. Al-HajriaManosh, C. P. Perumal Nithiarasu, S. Kumar, *Appl. Therm. Eng.* **2022**, *210*, 118339.

[7] M. A. S. R. Saadi, A. Maguire, N. T. Pottackal, M. S. H. Thankur, M. M. Ikram, A. J. Hart, P. M. Ajayan, M. M. Rahman, *Adv. Mater.* **2022**, *34*, 2108855.

[8] M. Coffigniez, L. Gremillard, M. Perez, S. Simon, C. Rigollet, E. Bonjour, P. Jame, X. Boulnat, *Acta Mater.* **2021**, *219*, 117224.

[9] ISO/ASTM 52900, *Additive Manufacturing — General Principles — Terminology*.

[10] J. Lewis, *Adv. Funct. Mater.* **2006**, *16*, 2193.

[11] M. Kachit, A. Kopp, J. Adrien, E. Maire, X. Boulnat, *J. Mater. Res. Technol.* **2022**, *20*, 1341.

[12] M. Yarahamadi, P. Barcelona, G. Fargas, E. Xuriguera, J. J. Roa, *Ceram. Int.* **2022**, *48*, 4775.

[13] L. Biasetto, H. Elsayed, *Adv. Eng. Mater.* **2022**, *24*, 2101729.

[14] M. Coffigniez, L. Gremillard, X. Boulnat, *Adv. Eng. Mater.* **2022**, *25*, 2201159.

[15] V. Lenaerts, C. Triqueneaux, M. Quartern, F. Rieg-Falson, P. Couvreur, *Int. J. Pharm.* **1987**, *39*, 121.

[16] A. A. Barba, M. d'Amore, M. Grassi, S. Chirico, G. Lamberti, G. Titomanlio, *J. Appl. Polym. Sci.* **2009**, *114*, 688.

[17] A. Gleadall, D. Visscher, J. Yang, D. Thomas, J. Segal, *Burns Trauma* **2018**, *6*, 19.

[18] A. M'Barki, L. Bocquet, A. Stevenson, *Sci. Rep.* **2017**, *7*, 6017.

[19] N. Novak, L. Biasetto, P. Rebesan, F. Zanini, S. Carmignato, L. Krstulović-Opara, M. Vesenjak, Z. Ren, *Addit. Manuf.* **2022**, *45*, 1022022.

[20] D. Prall, R. S. Lakes, *Int. J. Mech. Sci.* **1997**, *39*, 305.

[21] C. J. Dimitriou, R. H. Ewoldt, G. H. McKinley, *J. Rheol.* **2013**, *57*, 27.

[22] V. G. Rocha, E. Saiz, I. S. Tirichenko, E. Garcia-Tunon, *J. Mater. Chem. A* **2020**, *8*, 15646.

[23] M. Sweeney, L. L. Campbell, J. Hanson, M. L. Pantoya, G. F. Christopher, *J. Mater. Sci.* **2017**, *52*, 13040.

[24] A. Gleadall, *Addit. Manuf.* **2021**, *46*, 102109.

[25] J. Gao, M. Xiao, J. Yan, W. Yan, *Comput. Methods Appl. Mech. Eng.* **2020**, *362*, 112876.

[26] A. Sorrentino, D. Castagnetti, L. Mizzi, A. Spaggiari, *Mech. Mater.* **2022**, *173*, 104421.

[27] C. Soyarslan, A. Gleadall, J. Yan, H. Argeso, E. Sozumert, *Mater. Des.* **2023**, *226*, 111580.